# Absolute Atomic Oxygen Density Measurements by Two-Photon Absorption Laser-induced Fluorescence Spectroscopy in an RF-Excited Atmospheric Pressure Plasma Jet

INSTITUTE OF PHYSICS PUBLISHING PLASMA SOURCES SCIENCE AND TECHNOLOGY

Plasma Sources Sci. Technol. **14** (2005) 375–386 doi:10.1088/0963-0252/14/2/021

# Absolute atomic oxygen density measurements by two-photon absorption laser-induced fluorescence spectroscopy in an RF-excited atmospheric pressure plasma jet

**K Niemi**[1], **V Schulz-von der Gathen and H F Döbele**

Universität Duisburg-Essen, Fachbereich Physik, Universitätsstr. 5, 45117 Essen, Germany

E-mail: kari@iep.physik.uni-essen.de

Received 10 December 2004, in final form 21 March 2005
Published 21 April 2005
Online at stacks.iop.org/PSST/14/375

**Abstract**

The atmospheric pressure plasma jet is a capacitively coupled radio frequency discharge (13.56 MHz) running with a high helium flux (2 $m^3\,h^{-1}$) between concentric electrodes. Small amounts (0.5%) of admixed molecular oxygen do not disturb the homogeneous plasma discharge. The jet effluent leaving the discharge through the ring-shaped nozzle contains high concentrations of radicals at a low gas temperature—the key property for a variety of applications aiming at treatment of thermally sensitive surfaces. We report on absolute atomic oxygen density measurements by two-photon absorption laser-induced fluorescence (TALIF) spectroscopy in the jet effluent. Calibration is performed with the aid of a comparative TALIF measurement with xenon. An excitation scheme (different from the one earlier published) providing spectral matching of both the two-photon resonances and the fluorescence transitions is applied.

## 1. Introduction

Atmospheric pressure plasma sources are widely used for materials processing. The traditional sources like arcs and plasma torches providing thermal plasmas with high temperature are primarily used in metallurgy. Corona discharges and dielectric barrier discharges generate non-equilibrium plasmas with a low degree of ionization at intermediate gas temperatures. Their application is often limited due to their non-uniformity. This shortcoming may be overcome by recently developed discharges: the atmospheric pressure glow (APG) [1, 2] in dielectric barrier discharges and the atmospheric pressure plasma jet (APPJ) [3], the latter source being the object of this study.

The APPJ consists of an assembly of two electrodes, either in concentric or planar geometry, through which a high flux of helium with a small amount of molecular additives, e.g. $O_2$ or $CF_4$, is supplied. A diffuse plasma is generated in the inter-electrode gap by capacitively coupled RF power. The main interest concerns the properties of the jet effluent leaving the discharge through the nozzle.

Earlier investigations of the discharge characteristics of the APPJ include optical emission spectroscopy (OES), Langmuir probes and electrical measurements [4–7]. The results can be summarized as follows: the APPJ is an $\alpha$-mode capacitive RF discharge with a gas temperature below 200°C, electron densities from $10^{11}$ to $10^{12}$ $cm^{-3}$ and a mean electron energy of ~2 eV. This source provides efficient production of radicals and allows treatment of thermally sensitive materials.

Various applications of the APPJ have been demonstrated, as illustrated in [8]: etching of Kapton [9], tantalum [10], tungsten, and silicon dioxide [11]; deposition of silicon dioxide [12] and silicon nitride [13] films, and decontamination of chemical and biological warfare [14]. The etch and deposition rates obtained are comparable to those achieved in low pressure applications at much higher cost.

[1] Author to whom any correspondence should be addressed.

  

In the experiments mentioned above several indications were found that atomic radicals have the dominant influence for surface treatment, rather than metastables, other neutrals or ions. This point is supported by the work of Jeong *et al* [15], who performed axially resolved optical emission and ultraviolet (UV) absorption measurements of $O_2(a\,^1\Delta_g)$, $O_2(b\,^1\Delta_g^+)$ and $O_3$ densities in the effluent of a planar APPJ operated with $O_2$/He, and used the results as input for a chemical kinetic model also including ground state He and O atoms. The model predicts O atom densities near the nozzle in the range of 0.2 to $1.0 \times 10^{16}$ cm$^{-3}$, depending on operating conditions. Recombination with $O_2$ leading to the formation of $O_3$ is considered the main loss mechanism for O atoms.

OES gives direct access only to excited particles, and conclusions on the atomic ground state density (exceeding that of excited states by several orders of magnitude) require rather complex models of approximative character. Furthermore, OES only provides line-of-sight integrated information, unless tomographic methods (e.g. Abel inversion in the case of radial symmetry) are applied. Laser absorption spectroscopy (LAS) and laser-induced fluorescence spectroscopy (LIF) give direct access to the ground state (and metastable) populations. However, the former is again restricted to line-of-sight integration, whereas the latter can provide spatial resolution due to the angle between the laser beam and detection path.

LAS and LIF of light atoms (e.g. H, N, O, Cl and F) have to cope with the problem of generating the required tunable narrow bandwidth radiation in the vacuum UV (VUV) spectral range, where the corresponding resonances are located. Stimulated anti-Stokes Raman scattering in hydrogen gas allows us to generate the necessary probing radiation [16, 17]. These diagnostics represent, however, only a solution for low ground state densities, since the exciting VUV radiation will no longer be sufficiently transmitted through media at elevated pressure, i.e. the resonance transition becomes optically thick with increasing ground state density, first in the centre and then in the wings of the line profile. Another possible source of absorption are other particles not being probed, e.g. by molecular oxygen or nitrogen.

Two-photon absorption laser-induced fluorescence spectroscopy (TALIF) in the UV spectral range can overcome these problems. It can be realized with commercial laser systems on the basis of frequency mixing (e.g. SHG or THG) in nonlinear optical crystals. The two-photon absorption process differs from the corresponding single-photon process: it is considerably less efficient, the excitation rate scales with the square of the laser intensity (in the case of two-photon absorption from a single beam), and the optical selection rules are complementary [18]. Fluorescence can only occur to intermediate states, usually in the visible or near infrared spectral range, and not directly back to the ground state. TALIF is, therefore, much less prone to re-absorption. The methods of single-photon and two-photon LIF do not compete in general: the former is more sensitive and is restricted to low densities by the requirement of transmission to ground state densities $<10^{11}$ cm$^{-3}$, whereas TALIF covers the domain of medium density limited to the high density side by the problem of collision-induced quenching (i.e. collisional de-excitation).

Other sophisticated laser diagnostic methods providing direct access to ground state atoms in high pressure media have been developed in the frame of combustion and atmospheric research [19]. Attempts to detect atomic oxygen (its ground state exhibits triplet structure) in flames by Raman spectroscopy [20] and coherent anti-Stokes Raman spectroscopy (electronically resonant) [21] turned out to be difficult: the signals were strongly superimposed by molecular resonances. In contrast, two-photon resonant degenerated four-wave mixing [22, 23] is a promising technique, which seems to be independent of quenching. However, this method has not yet been proven, to the best of our knowledge, to be suitable for quantitative measurements. An alternative four-wave mixing technique is two-photon polarization spectroscopy [24], being both quench-free and quantitative. This concept has been applied successfully to atomic hydrogen.

We report on quantitative, spatially resolved TALIF measurements of atomic oxygen ground state densities in the effluent of an APPJ with concentric geometry, operated with $O_2$/He. The results are based on a TALIF calibration scheme with xenon providing better reliability and experimental simplicity compared to the one previously reported [25, 26]. We can infer the effective quenching rate on the basis of measured quenching coefficients, since in this particular situation we know the dominant colliders responsible for the strong and inhomogeneous quenching of the laser excited oxygen atoms—molecular oxygen and helium—as well as their density distributions.

This article is structured as follows: we describe, first, the principle of the calibration method and summarize the experimental set-up briefly. The preparatory measurements of the atomic data necessary for calibration are then described, followed by the experimental results obtained in the APPJ effluent. Finally, we summarize the results and discuss the outlook for the future.

## 2. TALIF calibration with noble gases

The method of TALIF calibration with noble gases for the determination of absolute atomic ground state densities has been introduced by Goehlich *et al* [25]. It represents a technically simple alternative to the use of atomic reference sources like the flow-tube reactor with titration [27]. The method is based on comparative TALIF measurements using a noble gas as a reference with a two-photon resonance spectrally close to that of the atomic species to be quantified. Xenon is well suited for the purpose of the present measurements—calibration of atomic oxygen—as shown in figure 1.

Several rules have to be observed: the conditions of excitation and detection should be as similar as possible for both the oxygen and xenon transitions; this includes the properties of the laser output and the optical set-up. Only the unsaturated quadratic signal response allows a quantitative comparison. The various saturation effects (ground state depletion, photo-ionization out of the excited state, amplified spontaneous emission (ASE) via fluorescence channels or artificial particle generation, e.g. by photodissociation) exhibit rather complex intensity dependences with individual thresholds; therefore, the laser intensity has to be kept as low as possible. The unknown

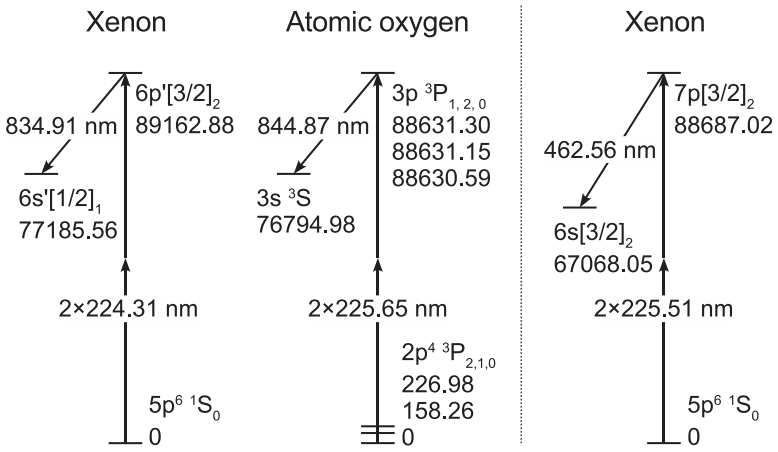


**Figure 1.** Matching two-photon excitation schemes of atomic oxygen and xenon (energies given in $cm^{-1}$, $J$-values ordered from lowest to highest energy and transitions denoted by vacuum wavelength).

atomic ground state density $n_X$ is then related to the reference gas density $n_R$ by

$$n_X = \frac{T_R \eta_R}{T_X \eta_X} \frac{\sigma_R^{(2)}}{\sigma_X^{(2)}} \frac{a_R}{a_X} \left(\frac{h\nu_X}{h\nu_R}\right)^2 \frac{S_X}{S_R} n_R = \chi \frac{S_X}{S_R} n_R \qquad (1)$$

with the 'normalized' fluorescence signal $S$ (integrated over fluorescence wavelength, excitation wavelength and interaction time, and normalized to the squared laser pulse energy), the photon energy $h\nu$, the effective branching ratio $a$ of the observed fluorescence transition, the transmission $T$ of the detection optics and the detector's quantum efficiency $\eta$ for the fluorescence wavelength, and the two-photon excitation cross section $\sigma^{(2)}$.

For low pressure media (collisionless case) the calibration factor $\chi$ depends only on atomic cross sections and experimental constants. With increasing pressure, the situation becomes more complex. Collisional quenching reduces the effective branching ratio of a spontaneous transition $i \rightarrow k$:

$$a_{ik} = \frac{A_{ik}}{A_i + Q_i} \qquad (2)$$

where $A_i = \sum_{k<i} A_{ik} = \tau_i^{-1}$ denotes the total spontaneous emission rate of the upper level, which is equal to its reciprocal radiative lifetime $\tau_i$, and $Q_i = \sum_q k_q^i n_q$ the effective quenching rate, which can be expressed by the collision partner densities $n_q$ and the corresponding quenching coefficients $k_q^i$. The collision partner densities depend on the gas temperature $T_g$ according to the ideal gas law as well as the quenching coefficients according to the kinetic theory. For a thermal velocity distribution, the following relation holds:

$$k_q^i = \sigma_q^i \langle v \rangle = \sigma_q^i \sqrt{\frac{8 k_B T_g}{\pi \mu}} \qquad (3)$$

with mean collision velocity $\langle v \rangle$, Boltzmann's constant $k_B$, reduced mass of the colliders $\mu$, and collision cross section $\sigma_q^i$, which generally exhibits a modest temperature dependence [28].

The fine structure of atomic oxygen has to be considered in the present case. The ground state and the two-photon excited state are triplet states. The splitting of the excited state ($0.7\,cm^{-1}$) can only be resolved partially with respect to the room temperature Doppler width ($0.274\,cm^{-1}$) in contrast to the substantial ground state splitting ($227\,cm^{-1}$), which is comparable to the mean kinetic energy at room temperature ($k_B T_g = 209\,cm^{-1}$ for $T_g = 300\,K$). If the ground state exhibits a thermal population distribution, only one ground state sub-level (with total angular momentum quantum number $J$ and energy $E_J$) has to be probed in order to determine the total ground state population by considering the corresponding Boltzmann population fraction:

$$\frac{n_J}{\sum_J n_J} = \frac{(2J+1)\exp(-E_J/k_B T_g)}{\sum_J (2J+1)\exp(-E_J/k_B T_g)}. \qquad (4)$$

Note that equation (1) does not include polarization effects, which can lead to an anisotropic fluorescence radiation pattern, i.e. an anisotropic distribution of the fractional amount of the fluorescence intensity in the direction of detection as a function of the angle to the direction of polarization of the exciting radiation, as observed in [29]. In the case of single-photon LIF in low-pressure media, these effects are well known and calculable on the basis of quantal angular momentum coupling [30, 31]. In the case of TALIF they are nontrivial to calculate, since intermediate (and continuum) states of different angular configurations contribute (nonresonantly) to the two-photon absorption process, so that their weighting depending on the radial matrix elements has to be evaluated to determine the distribution of the magnetic quantum numbers $m_J$ in the excited state and the resulting polarization characteristics. Yet another difficulty is the theoretical treatment of depolarizing ($m_J$-changing) collisions leading to an enhanced degree of isotropy at elevated pressure. In such a situation an experimental verification represents a more convenient alternative.

The applicability of the calibration method requires a knowledge of atomic data, namely the radiative lifetimes and the corresponding quenching coefficients of the laser-excited states as well as the two-photon excitation cross-section ratio. For calibration of atomic oxygen using the reference scheme of xenon shown in figure 1 on the right-hand side [25], as well as for atomic hydrogen and nitrogen with krypton [26], the relevant quantities have already been provided—the measurement was based on flow-tube reactors in which the

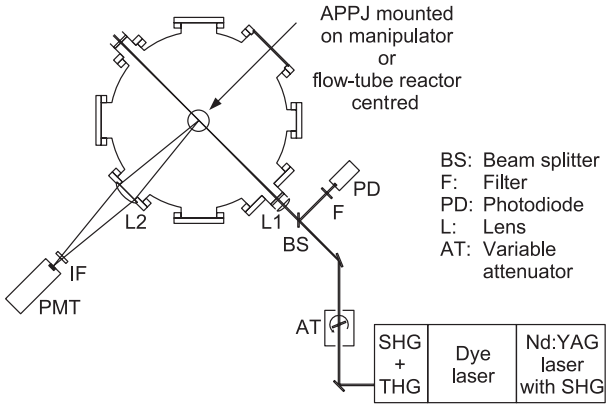


**Figure 2.** Scheme of the TALIF set-up.

atomic density had been determined by titration. The accuracy of the resulting values for the cross-section ratios was estimated to be 50%.

We chose a different calibration scheme for atomic oxygen—see the scheme on the left in figure 1—providing spectral matching of the two-photon resonances as well as of the fluorescence transitions. Because both fluorescence wavelengths can be detected by using the same interference filter and a red-sensitive photomultiplier, the errors in determining the detection sensitivity are significantly reduced, resulting in improved reliability and experimental simplification.

## 3. Experimental

An overview of the experimental set-up is shown in figure 2. The experiment is performed in a chamber (51 cm diameter, 45 cm height) in order to have well-defined conditions concerning gas flux and ambient environment. The plasma jet is mounted on a stepper-motor-controlled manipulator that allows three-dimensional displacements with respect to the fixed optical diagnostic beams. The gas flow associated with jet operation is guided from the centre of the top flange by a large diameter hose to the laboratory exhaust, so that symmetric flow conditions are warranted. For the preparatory measurements with the flow-tube reactor the latter is attached to an inclined top port (28° with respect to the chamber axis) so that the exit of the main flow-tube is located at the centre of the chamber. The exhaust port is then closed and the chamber is evacuated through the bottom flange by a rotary pump equipped with a throttle valve in order to establish a well-controllable gas flow.

### *3.1. TALIF set-up*

The commercial laser system (Continuum) consists of a dye laser (ND6000, equipped with dual 2400 grooves $mm^{-1}$ gratings). It is pumped by a frequency-doubled Nd : YAG laser (Powerlite 8000) at $\lambda = 532$ nm with a repetition rate of 10 Hz. The output radiation at $\lambda = 673$–$677$ nm is frequency-doubled and tripled with the aid of KD*P and BBO crystals, respectively; both crystals are automatically tracked while scanning the dye laser. Only half of the Nd : YAG laser output energy of 850 mJ in 6 ns is applied to pump the dye laser in order to ensure narrow bandwidth ($\sim 0.1\,cm^{-1}$) UV pump radiation; the pulse energy and duration are 4 mJ and 5 ns, respectively. The dye laser performs an automatic wavelength calibration during start-up; the accuracy of this calibration is about $\pm 0.002$ nm for the fundamental dye laser wavelength. As a result, the calculated two-photon wavenumber scales of the two-photon excitation spectra shown in this contribution may be shifted up to $0.6\,cm^{-1}$ against each other. We assume the same excitation conditions for xenon and atomic oxygen, because the conditions of generation and amplification of the dye laser radiation are comparable, since the required wavelengths are located in the central part of the broad tuning range (full width of $\Delta\lambda = 37$ nm at 90% of the maximum value at $\lambda_0 = 679$ nm) of the dye—a mixture of DCM and Pyridin1 in methanol.

The UV radiation is guided by dielectric mirrors and is focused to the centre of the experimental chamber by Suprasil optics—an $f = 40$ cm spherical lens or an $f = 35$ cm cylindrical lens oriented to produce a horizontal focal line. The focal region is imaged transverse to the laser beam by a BK7 lens ($f = 12.5$ cm, $\varnothing = 8.5$ cm) onto the photocathode of a red-sensitive PMT (Burle C31034A, modified for pulsed operation) through an interference filter ($\lambda_0 = 842$ nm, $\Delta\lambda_{FWHM} = 19$ nm). The UV pump energy is monitored with a fast photodiode. The fluorescence signal and the reference signal are recorded by a digital sampling oscilloscope (400 MHz, 2 Gs $s^{-1}$). A variable attenuator was inserted into the UV beam in order to study the fluorescence signal response. The attenuator consists of a dielectrically coated thin Suprasil substrate whose inclination is controlled by a stepper-motor, whereby attenuation is achieved according to the angular dependence of the reflection properties of the coating. Within the working range, about 6° rotation, the beam displacement and direction change is negligible.

### *3.2. The flow-tube reactor*

The flow-tube reactor is shown schematically in figure 3. A mixture of molecular oxygen in helium or argon (typ. 1 : 100) is admitted through the quartz tube ($\varnothing = 9$ mm) placed in the centre of the microwave resonator. O atoms are generated in the microwave discharge (2.45 GHz, 50 W) by electron impact dissociation. The total gas flux expands into the main flow-tube ($\varnothing = 19$ mm) made of Teflon to minimize wall recombination losses (typ. rate $50\,s^{-1}$). The atoms in the carrier gas are transported to the detection volume located 45 cm downstream of the discharge and accessible through holes in the flow-tube. The distance between the discharge and the location of the detection volume provides sufficient relaxation and thermalization of the gas mixture under typical operational conditions: total gas flux of 700 sccm at a total pressure of 1000 Pa. All gas flows are monitored by mass flow controllers, and the total flux is controlled by a throttle valve; the total pressure is monitored by a capacitive pressure gauge. The mean flux velocity is estimated to be 4 m $s^{-1}$ and the Reynolds number to be 6 (for helium), which is definitely in the regime of laminar flow. Radial gradients of the radical density are negligible over the flow-tube cross section under the conditions stated, as demonstrated in [32]. A narrow Teflon tube orifice in the flow-tube located 5 cm upstream of the detection volume allows us to add other gases to the main flux in a controlled

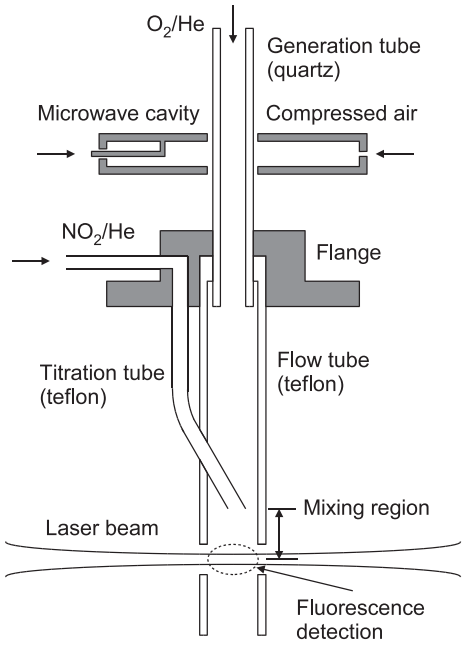


**Figure 3.** Scheme of the flow-tube reactor.

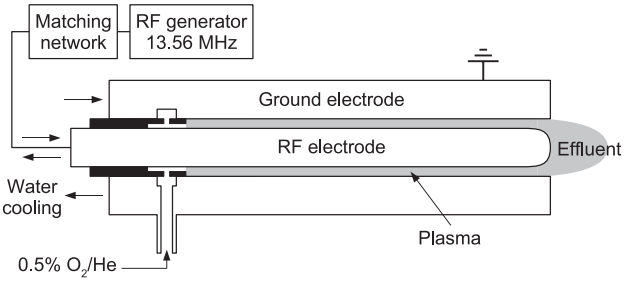


**Figure 4.** Cross-sectional view of the APPJ.

manner, e.g. for the titration procedure a $NO_2$/He premix, or for lifetime and quenching coefficient measurements a suitable collision partner gas.

### *3.3. The atmospheric pressure plasma jet*

Figure 4 shows the scheme of the plasma jet used in this study. This plasma source consists of two concentric stainless steel electrodes, both water cooled (140 litre $h^{-1}$). The Teflon tube spacer—also acting as an insulator, seal and diffuser for the feed gas—warrants a uniform electrode spacing of 2 mm ($\varnothing = 10$ and 14 mm). The effective electrode length amounts to 10 cm. RF power (13.56 MHz), up to 200 W, is applied through a Π-matching network to the inner electrode, whereas the outer electrode is grounded. The working gas, a mixture of helium and oxygen, is supplied via variable area flow meters. For a helium flux of 0.5–2 $m^3\,h^{-1}$ with molecular oxygen admixtures up to 1% a stable homogeneous plasma is obtained. The faint jet effluent leaving the nozzle is visible over a distance of slightly more than one centimetre. If the power limits stated are not observed, or if the oxygen admixture is in excess—the latter scales with flow rate and power—then arcing occurs at the edge of the nozzle. For a helium flux of 2 $m^3\,h^{-1}$ the flux velocity $\bar{v}$ is estimated to be 7.4 m $s^{-1}$. An estimation of the

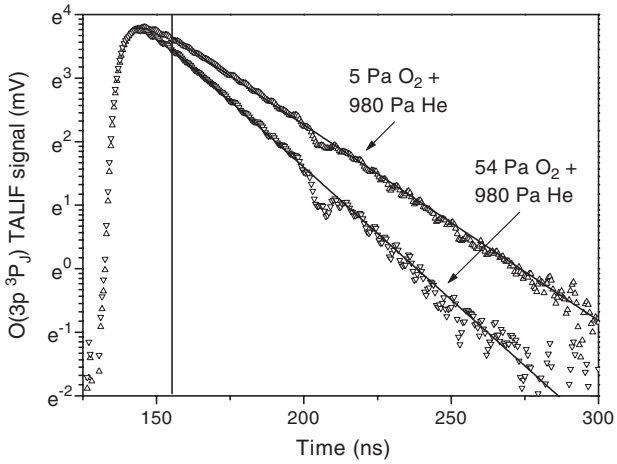


**Figure 5.** Time-resolved $O(3p\,^3P_J)$ TALIF signals obtained with and without admixture of $O_2$.

Reynolds number $Re = d\bar{v}\rho/\eta$ with the gap width $d = 2$ mm, the density $\rho_{He}(10^5\,\text{Pa}, 300\,\text{K}) = 1.6 \times 10^{-4}\,\text{g cm}^{-3}$ and the dynamic viscosity $\eta_{He}(300\,\text{K}) = 2 \times 10^{-6}\,\text{Pa s}$ yields a value of 118, which is well within the laminar flow regime in view of the fact that the transition to the turbulent regime usually occurs at $Re > 1700$–2300.

## 4. Preparatory measurements at the flow-tube reactor

### *4.1. Radiative lifetimes and quenching coefficients*

A precise knowledge of the radiative lifetimes and the corresponding quenching coefficients of the (two-photon excited) $O(3p\,^3P)$ and $Xe(6p'[3/2]_2)$ atoms is required to perform reliable quantitative measurements in the APPJ effluent according to the TALIF calibration scheme proposed. Although the necessary data are available in principle, we decided to determine them again on an improved basis, because some published data exhibit large uncertainties or even disagreement beyond the stated errors.

We generate O-atoms in the flow-tube reactor at a constant feed gas flux and introduce a variable flux of an additional quencher, either He or Ar through the discharge, or $O_2$ through the titration tube. As an example, two fluorescence signal waveforms obtained with and without an additional $O_2$ admixture are shown in figure 5. After termination of the laser pulse (5 ns FWHM) the signals follow closely a single exponential decay within 10 ns as indicated by the vertical line (the dip in the figure at ∼200 ns is an artefact of the PMT response). The corresponding decay rates $A^*$, derived by an unweighted exponential fitting procedure, are plotted versus the partial pressure of the admixed quencher as shown in figure 6. From this so-called Stern–Volmer plot the quenching coefficients $k$ are deduced from the slopes as well as the radiative lifetime $\tau$ from the zero-pressure intercepts according to

$$A^* = \frac{1}{\tau} + k_{O_2} n_{O_2} + k_{He,Ar} n_{He,Ar}. \qquad (5)$$

For the evaluation of the quenching coefficients Dalton's law is applied assuming room temperature (300 K). This has been

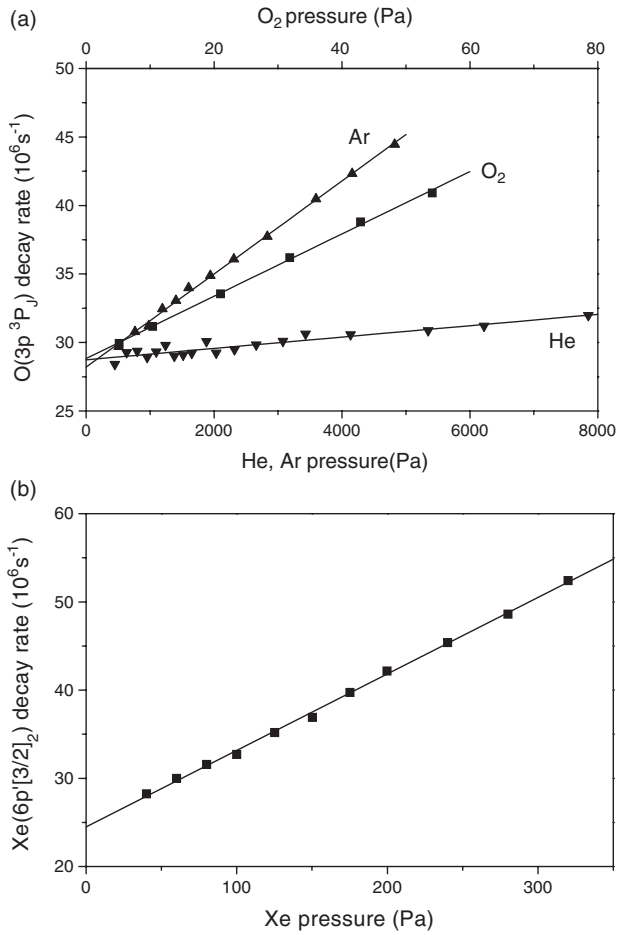


**Figure 6.** (*a*) Decay rate of $O(3p\ ^3P_J)$ atoms versus partial pressure of $O_2$, Ar and He; results corrected for background quenching by the feed gas. (*b*) Decay rate of $Xe(6p'[3/2]_2)$ atoms versus xenon pressure.

verified experimentally, as shown later. Real-gas-factors for the gases used are not taken into account; their deviation from unity is estimated to be below 1% within the pressure range applied in this study.

Note that 'self-quenching' of excited O atoms by ground state O atoms is neglected, because atomic oxygen is a minority species in our case and is, in addition, a rather inefficient quencher according to Dilecce *et al* [33], who derived an upper limit of $0.82 \times 10^{-10}$ cm$^3$ s$^{-1}$ for the self-quenching coefficient from TALIF measurements in an oxygen plasma jet having a sufficiently high and controllable degree of dissociation.

The self-quenching coefficient of $Xe(6p'[3/2]_2)$ atoms can be measured in a straightforward manner: we switch the flow-tube reactor off and repeat the measurement procedure at various xenon filling pressures; the corresponding Stern–Volmer plot is included in figure 6.

The results are summarized in table 1 and compared with published data. The values for the lifetimes are in good agreement with the references. When looking at the quenching coefficients, an obvious trend is observed: the less efficient the quencher, the larger is the deviation among the data. The reason is that a small lifetime change caused by an inefficient quencher is difficult to measure, and the risk of interference by strongly quenching gas impurities is rather high. In particular,

**Table 1.** Radiative lifetimes and room temperature quenching coefficients of $O(3p\ ^3P_J)$ and $Xe(6p'[3/2]_2)$ atoms.

| | Radiative lifetime (ns) | |
|---|---|---|
| Excited state | This work | Others |
| $O(3p\ ^3P_J)$ | $34.7 \pm 1.7$ | $35.1 \pm 3.0$[a] |
| | | $36.2 \pm 0.7$[b] |
| $Xe(6p'[3/2]_2)$ | $40.8 \pm 2.0$ | $40 \pm 6$[c] |
| | | $37 \pm 2$[d] |
| | Quenching coefficient ($10^{-10}$ cm$^3$ s$^{-1}$) for $O(3p\ ^3P_J)$ atoms | |
| Reagent | This work | Others |
| $O_2$ | $9.4 \pm 0.5$ | $9.3 \pm 0.4$[a] |
| | | $6.3 \pm 0.1$[b] |
| | | $8.6 \pm 0.2$[e] |
| Ar | $0.14 \pm 0.007$ | $0.25 \pm 0.08$[a] |
| | | $0.21 \pm 0.07$[b] |
| He | $0.017 \pm 0.002$ | $0.07 \pm 0.02$[a] |
| | | $0.15 \pm 0.05$[b] |
| | Self-quenching coefficient ($10^{-10}$ cm$^3$ s$^{-1}$) for $Xe(6p'[3/2]_2)$ atoms | |
| Reagent | This work | Others |
| Xe | $3.6 \pm 0.4$ | $4.2 \pm 0.5$[c] |
| | | $4.3 \pm 0.1$[f] |

[a] [26]. [b] [34]. [c] [35]. [d] [36]. [e] [37]. [f] [38].

we believe that our values for the O*+Ar and O*+He quenching coefficients are the most reliable, because our measurement was performed over the largest possible pressure range, up to 50 and 80 mbar, respectively, until the microwave discharge switched to an unstable constricted mode.

### *4.2. Two-photon excitation cross sections*

The two-photon excitation cross section of the $O(2p^4\ ^3P_J \rightarrow 3p\ ^3P_J)$ resonance has been determined both experimentally and theoretically—see [37] and references [41–43] given there. To the best of our knowledge no data exist, however, for the $Xe(5p^6\ ^1S_0 \rightarrow 6p'[3/2]_2)$ resonance. We determined, therefore, the ratio of these two-photon excitation cross sections according to the calibration scheme shown above on the basis of comparative TALIF measurements with defined xenon and atomic oxygen densities, the latter being generated in the flow-tube reactor and quantified by titration.

The absolute atomic oxygen density in the flow-tube reactor is determined by titration according to the reaction given below, where we also give the pertinent room temperature rate constant $k_T$ [27]:

$$O + NO_2 \rightarrow NO + O_2, \qquad k_T = 9.5 \times 10^{-12}\ \text{cm}^3\ \text{s}^{-1}. \quad (6)$$

The titration gas, an $NO_2$/He premix with an $NO_2$ fraction of 1.47% as determined by FTIR spectroscopy, is added through the titration tube 5 cm upstream of the detection volume to the main flux. The on-resonance TALIF signal is measured as a function of the titration gas flux as shown in figure 7.

Since each $NO_2$ molecule leads to the consumption of one O atom under the assumption of ideal mixing and complete reaction before detection, the signal decreases linearly with increasing titration gas flux until the signal amplitude tends to

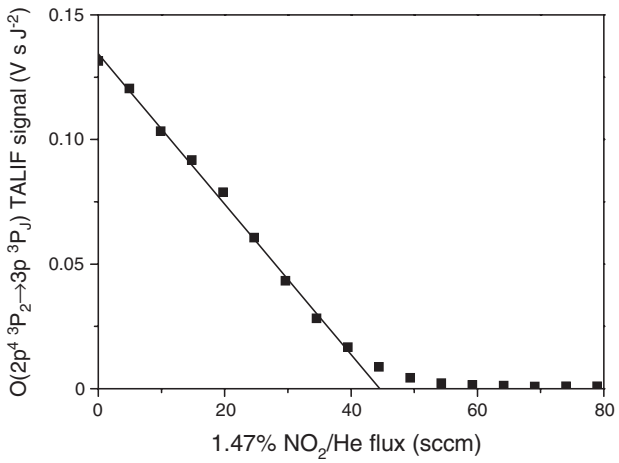


**Figure 7.** Measured titration curve for 705 sccm He and 3.5 sccm $O_2$ fluxes at 985 Pa total pressure and 50 W microwave power.

zero. At this so-called 'titration endpoint' the $NO_2$ flux $\phi^{(T)}_{NO_2}$ equals the initial O atom flux, so that the corresponding O atom density $n_O$ can be obtained according to Dalton's law

$$n_O = \frac{\phi^{(T)}_{NO_2}}{\phi_{tot}} n_{tot} \simeq \frac{\phi^{(T)}_{NO_2}}{\phi_{tot}} \frac{p}{k_B T_g} \tag{7}$$

with the total gas flux $\phi_{tot}$, the total pressure $p$ and the gas temperature $T_g$.

There are several rules to be observed in the titration procedure. Some have already been mentioned in the experimental part: laminar flow conditions in the main tube, low recombination losses along the reaction path and conditions under which radial density gradients over the flow-tube cross section are negligible. Another obvious condition is, that the (variable) titration gas flux has to be small compared with the main flux to warrant a constant radical production at stable discharge conditions. We also have to make sure that the titration reaction is complete before the flow reaches the focus.

The reaction occurs according to

$$\frac{d}{dt} n_O = \frac{d}{dt} n_{NO_2} = -k_T n_O n_{NO_2} = v \frac{d}{dx} n_O = v \frac{d}{dx} n_{NO_2}, \tag{8}$$

where the flux velocity $v = x/t$ connects the coordinates of the particles transported from the point of admixture to the point of detection. For equal initial densities $n_O(0) = n_{NO_2}(0)$ we get the particular solution corresponding to the titration endpoint:

$$n_O(t) = \frac{n_O(0)}{1 + k_T n_O(0) t}. \tag{9}$$

Obviously, the condition $k_T\, n_O(0)\, t \gg 1$ has to be fulfilled in order to reach complete reaction and, consequently, a well-defined titration endpoint. On the other hand, the reaction time $t$ chosen should not be too large to avoid detrimental slower wall or secondary reactions, e.g. $O + NO + M \rightarrow NO_2^* + M$ followed by $NO_2^* \rightarrow NO_2 + h\nu$ causing the so-called air afterglow.

The gas temperature required for the evaluation can be derived from a spectral scan over the O atom fine structure, shown in figure 8. A superposition (solid curve) of Voigt

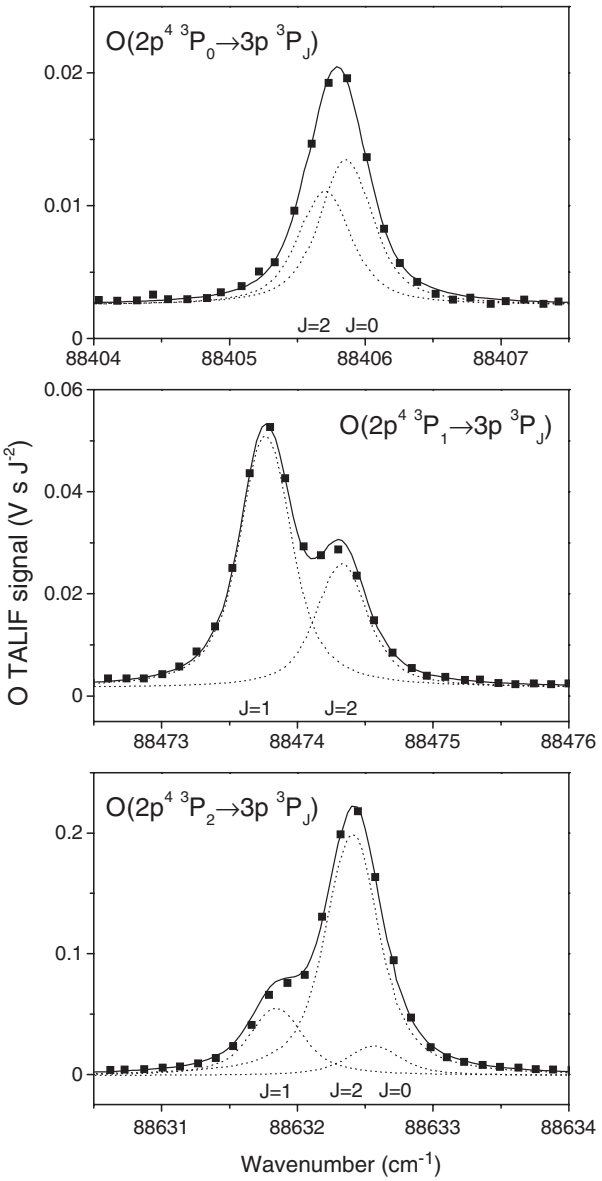


**Figure 8.** Two-photon excitation line profiles of the $O(2p^4\,{}^3P_{2,1,0} \rightarrow 3p\,{}^3P_{1,2,0})$ fine structure components. Solid and dotted curves are best fits to the measuring points; for details see text.

profiles (dotted curves) were fitted to the measuring points using numerical methods from [39, 40]. The weighting (table IX, column 3 of [41]) and relative displacement of the components were fixed to the theoretical values. Besides an amplitude factor and the absolute spectral position, the shared Gaussian and Lorentzian widths were varied. The fluorescence intensity (spectrally integrated over the upper three sub-levels) yields the population distribution over the lower sub-levels. The corresponding Boltzmann plot is shown in figure 9. From the slope of this plot we obtain a temperature of $(300 \pm 30)$ K. This is a clear indication of sufficient relaxation and thermalization of the O atoms within the cold carrier gas at the point of detection (far away from the microwave discharge).

For the titration curve shown in figure 7, the titration endpoint was derived by extrapolation of the signal amplitude as $\phi^{(T)}_{NO_2} = (0.655 \pm 0.025)$ sccm. We obtain from

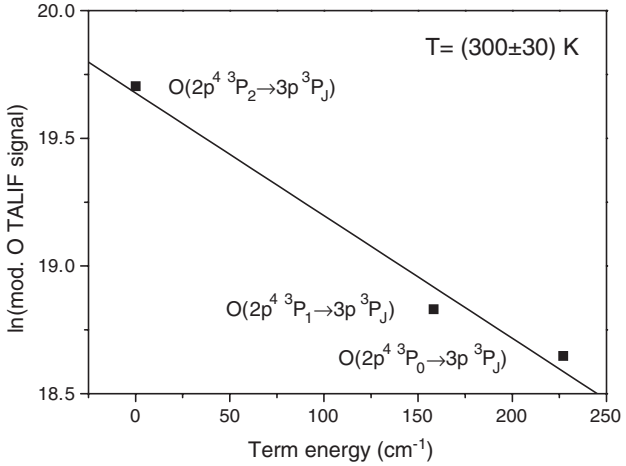


**Figure 9.** Boltzmann plot of the population distribution over the sub-levels of the atomic oxygen ground state.

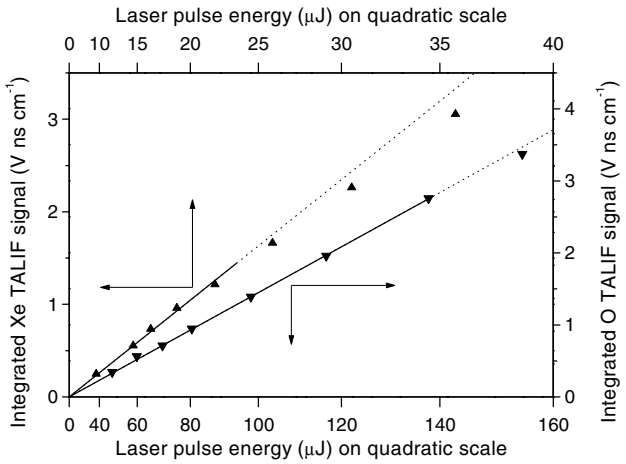


**Figure 10.** Example for comparative TALIF measurements; for details see text.

equation (7), together with the stated operational parameters, a total atomic oxygen density of $(2.2 \pm 0.1) \times 10^{14}\,\mathrm{cm}^{-3}$ and, according to equation (4), a population density of $(1.63 \pm 0.07) \times 10^{14}\,\mathrm{cm}^{-3}$ for the usually probed $2p^4\,{}^3P_2$ sub-level. The result allows us to verify the criterion for completion of the titration reaction mentioned before. With the estimated reaction time $t = 12\,\mathrm{ms}$ (connected with the total flux, the flow-tube cross section and the reaction length) the product $k_T n_O(0)\,t$ assumes a value of 25, supporting the reliability of the results.

A series of comparative TALIF measurements was performed at the calibrated flow-tube reactor with static xenon filling pressure, in order to determine the ratio of the two-photon excitation cross sections. Figure 10 shows exemplarily the (temporally and spectrally) integrated $O(3p\,{}^3P_J)$ TALIF signal obtained at the $O(2p^4\,{}^3P_2)$ population density of $(1.63 \pm 0.07) \times 10^{14}\,\mathrm{cm}^{-3}$ as a function of the laser pulse energy in comparison to the integrated $Xe(5p^6\,{}^1S_0 \rightarrow 6p'[3/2]_2)$ TALIF signal obtained at a xenon pressure of 10 Pa. Note the low threshold for the onset of saturation for xenon at about 25 $\mu$J—probably due to ASE in view of the small Doppler width [44]—in comparison to that of atomic oxygen

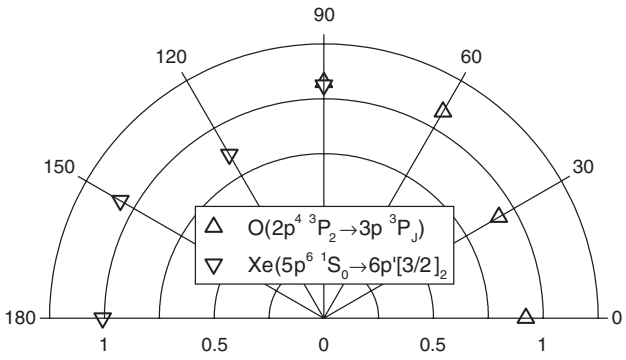


**Figure 11.** Fluorescence radiation pattern (normalized to unity).

at about 150 $\mu$J. In the chosen representation, each curve has an individual quadratic energy scale and the measuring points that follow (at small energy) the unsaturated quadratic signal response, are fitted by a line through the origin, whereas the others are disregarded. The slopes of these lines correspond to the 'normalized' TALIF signals as introduced in equation (1), from which the calibration factor $\chi$ can now be found.

The fluorescence radiation patterns of xenon and atomic oxygen have been measured: the horizontal direction of linear polarization of the exciting radiation was rotated with the aid of two air-spaced Rochon polarizers (Halle PLQ15) while keeping the energy of the transmitted laser radiation constant. The results of the measurements are shown in figure 11. They are subject to a rather large error due to beam displacement by the polarizers; the characteristics of the fluorescence intensity obtained are both in agreement with an isotropic distribution.

The detection sensitivity for both fluorescence wavelengths ($\lambda_{Xe} = 834.9\,\mathrm{nm}$, $\lambda_O = 844.9\,\mathrm{nm}$) is nearly equal according to manufacturer's data for the photomultiplier quantum efficiency ($\eta_{Xe} = 13.1\%$, $\eta_O = 12.5\%$) and the transmission of the interference filter ($T_{Xe} = 75.5\%$, $T_O = 84.5\%$). The effective optical branching ratios are calculated according to equation (2) on the basis of the measured lifetimes and quenching coefficients (table 1); the pure optical branching ratio ($A_{ik}/A_i$, $Q_i = 0$) for the atomic oxygen transition $3p\,{}^3P_J \rightarrow 3s\,{}^3S$ is unity, whereas for the xenon transition $6p'[3/2]_2 \rightarrow 6s'[3/2]_1$ the value 0.733 from [45] is used.

With these data, we derived the two-photon excitation cross-section ratio $\sigma^{(2)}(Xe)/\sum_{J'} \sigma^{(2)}_{J\rightarrow J'}(O) = 1.9$ from the measured calibration factor, where $J'$ is the total angular momentum quantum number of the upper fine structure levels; we estimate the overall uncertainty to be ~20%.

## 5. Investigation of the APPJ effluent

### *5.1. Laser-induced particle generation*

The TALIF measurements at the APPJ effluent were tackled with the same optical set-up as for the investigations at the flow-tube reactor, i.e. focusing the laser radiation was performed with an $f = 40\,\mathrm{cm}$ spherical quartz lens. A TALIF signal response increasing steeper than quadratic—up to a power of 3.5—was obtained in this case. This is an indication of laser-induced generation of O atoms, probably by

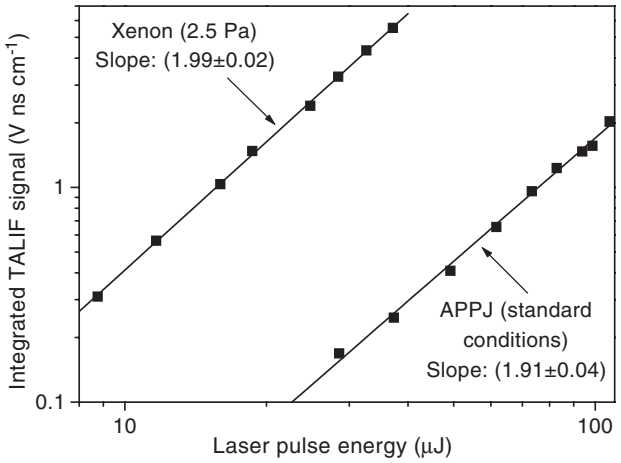


**Figure 12.** Measured TALIF signal response for atomic oxygen in the jet effluent and xenon using a cylindrical focusing lens.

photodissociation from ozone or metastable molecular oxygen. High concentrations of both species are expected to exist in the jet effluent [15]. We did not observe, however, any indication of 'hot' O atoms from the wings of the two-photon excitation line profile associated with photodissociation, in which the rather large excess energy is transferred to the fragments, particularly to the light atomic ones [46, 47]. The problem of artificial particle generation for quantitative density measurements could be circumvented (as demonstrated in figure 12) by replacing the plano-convex focusing lens with an $f = 35\,\mathrm{cm}$ cylindrical quartz lens oriented to produce a horizontal focal line. All TALIF measurements (in the jet effluent or at xenon filling pressures of a few Pa) presented in the following have been taken in the regime of quadratic signal response with this modified set-up.

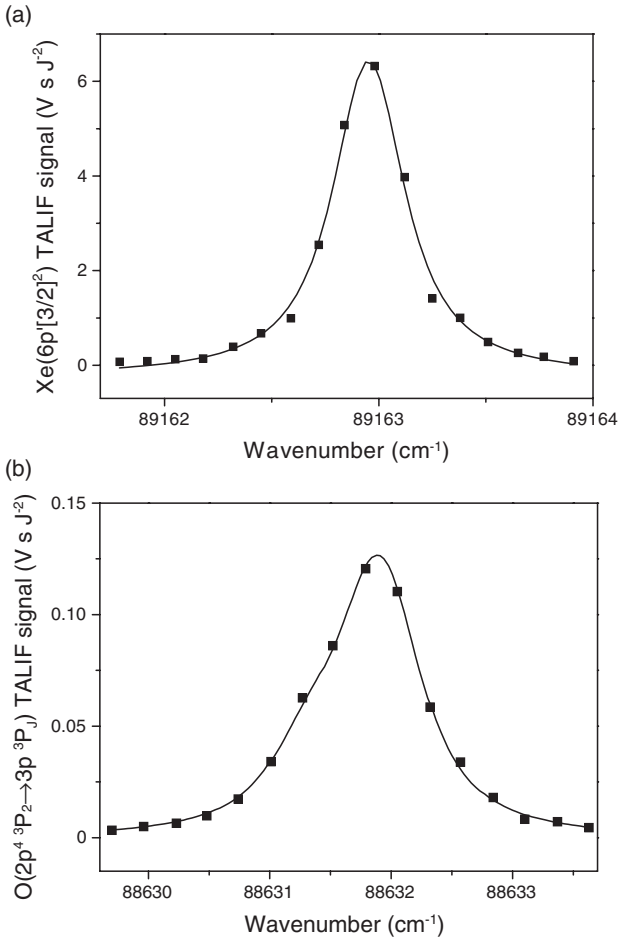


**Figure 13.** Two-photon excitation line profiles. (*a*) $\mathrm{Xe}(5p^6\,{}^1S_0 \rightarrow 6p'[3/2]_2)$ resonance; (*b*) $\mathrm{O}(2p^4\,{}^3P_2 \rightarrow 3p\,{}^3P_J)$ resonance obtained in the jet effluent. Solid curves are best fits; for details see text.

### *5.2. Pressure broadening*

In the following, we present results of spectral line shape analysis using the numerical methods of [39, 40] and keeping up the convention to give FWHM values.

Figure 13(*a*) shows a measured two-photon excitation line profile of the $\mathrm{Xe}(5p^6\,{}^1S_0 \rightarrow 6p'[3/2]_2)$ resonance. The solid curve is a Voigt profile adapted to the measuring points. We consider it to be composed of a Gaussian contribution determined by room temperature (Doppler width of xenon $0.096\,\mathrm{cm}^{-1}$) so that the Lorentzian contribution has an associated width of $0.19\,\mathrm{cm}^{-1}$. From the good agreement obtained with this fit we conclude that this Lorentzian contribution represents the effective (two-photon excitation) laser line profile. This indicates that the resulting profile including convolution is caused by a bandwidth of the laser radiation of $0.095\,\mathrm{cm}^{-1}$—actually about three times the bandwidth of the dye laser fundamental of $0.032\,\mathrm{cm}^{-1}$ as obtained by optogalvanic measurements. The apparent Lorentzian line shape of the dye laser output is reasonable in view of the short pulse duration of 5 ns during which only 2–3 full resonator passes are possible.

Figure 13(*b*) shows a two-photon excitation line profile of the $\mathrm{O}(2p^4\,{}^3P_2 \rightarrow 3p\,{}^3P_J)$ resonance obtained in the jet effluent. The solid curve is a superposition of Voigt profiles to the measuring points, each for one fine structure component, adapted according to their theoretical weight (table IX, column 3 of [41]) and relative spectral position. The best fit—shown in the figure—is obtained for a Gaussian contribution $0.296\,\mathrm{cm}^{-1}$ wide for the O atoms corresponding to a gas temperature of $T \sim 350\,\mathrm{K}$ measured by a thermocouple, as shown later. The resulting Lorentzian contribution of width $0.34\,\mathrm{cm}^{-1}$ is much broader, however, than the instrumental width derived from the line shapes of xenon, as discussed before, and of atomic oxygen in the flow-tube reactor; see figure 4. We conclude, therefore, that the $\mathrm{O}(2p^4\,{}^3P_2 \rightarrow 3p\,{}^3P_J)$ resonance is subject to a significant pressure broadening of $\sim 0.15\,\mathrm{cm}^{-1}$ in the jet effluent. Note that pressure broadening comprises both elastic and inelastic 'quenching' collisions. It is, therefore, not possible to determine effective quenching rates from the line width. As in our case, pressure broadening can screen the Doppler broadening, so that a reliable determination of the gas temperature from line width measurements is no longer possible. Note that a possible pressure shift of the $\mathrm{O}(2p^4\,{}^3P_2 \rightarrow 3p\,{}^3P_J)$ resonance cannot be inferred from our results in view of the uncertainty of the wavelength calibration as described in section 3.1.

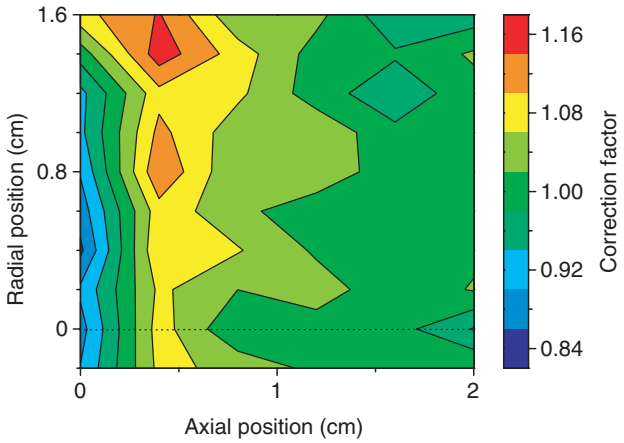


**Figure 14.** Correction factor for vignetting and reflection; for details see text.

### *5.3. Vignetting and reflection*

The solid angle of detection is apparently partially shadowed by the jet nozzle, if the fluorescence measurement is performed close to this object. The effective fluorescence yield is influenced by both vignetting and reflection at the nozzle surface. A homogeneous particle density is established by filling the experimental chamber with xenon (it has an isotropic fluorescence radiation pattern like atomic oxygen). The corresponding spatially resolved TALIF measurements (performed at constant laser pulse energy) yield the correction factor as shown in figure 14. In this map, as in the following ones, the axial zero position corresponds to the position from which the laser beam does not 'touch' the nozzle; the radial zero position corresponds to the jet axis as indicated by the dotted line. The radial scan corresponds to a lateral displacement of the jet in the opposite direction to the detection path (the side of less vignetting).

### *5.4. Collisional quenching and temperature dependent effects*

The majority species in the jet effluent are the feed gases: molecular oxygen and helium. They represent the dominant colliders responsible for the strong and inhomogeneous quenching of the laser-excited O atoms. The effective quenching rate can be calculated as outlined in section 2 on the basis of the measured room temperature quenching coefficients (table 3) and the measured gas temperature field shown in figure 15(*a*). The density distributions of both colliders are simply related to the gas temperature according to Dalton's law for the case of constant (atmospheric) pressure and constant ratio of molecular oxygen to helium (according to the feed gas composition) throughout the jet effluent. The former is supported by the laminar flow conditions and the latter by the fact that we have a cold and weakly dissociated gas in which the (plasma-)chemically generated particles are still in a minority. A knowledge of the gas temperature also allows us to account for the temperature dependence of the quenching coefficients as well as for the Boltzmann population fraction for the probed $O(2p^4\,{}^3P_2)$ ground state sub-level.

The gas temperature was measured by a thermocouple (K-type, dimensions $\sim$1 mm$^3$, ungrounded), which was inserted through an inclined top port (45° with respect to the chamber axis and perpendicular to the direction of the lateral displacement of the jet); the cable connection to the thermocouple was guided in a quartz glass tube except for the last 4 cm. In this configuration, the perturbation of the gas flow is minimal. Indications for an interference by the RF field were not found.

### *5.5. Absolute density measurements*

The determination of the absolute atomic density is performed in the following way: in a first step, a two-dimensional fluorescence map of the jet effluent is recorded, where the on-resonance $O(2p^4\,{}^3P_2 \rightarrow 3p\,{}^3P_2)$ fluorescence signal is measured as a function of the axial and radial positions scanned in increments of 4 mm and 2 mm, respectively. Then, the calibration measurement is performed at one spatial position, namely on-axis at a distance of 2 cm. The spectrally and temporally integrated $O(2p^4\,{}^3P_2 \rightarrow 3p\,{}^3P_J)$ fluorescence signal is measured as a function of the laser pulse energy. The analogous procedure is repeated for the case of xenon filling at the close-by $Xe(5p^6\,{}^1S_0 \rightarrow 6p'[3/2]_2)$ resonance. The fluorescence map data recorded on-resonance were converted into spectrally integrated data using the measured temperature distribution; pressure broadening was found to be space independent. The other individual corrections, as mentioned above, for collisional quenching, Boltzmann population fraction, vignetting and reflection are then applied

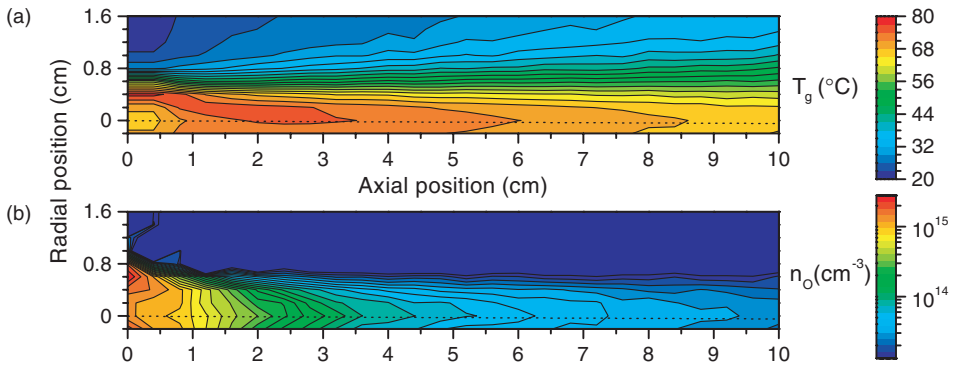


**Figure 15.** Gas temperature field (*a*) and map of absolute atomic oxygen density (*b*) in the APPJ effluent for 2 m$^3$ h$^{-1}$ He and 0.01 m$^3$ h$^{-1}$ $O_2$ fluxes and 150 W RF power.

to all measuring points. The resulting map of the absolute atomic oxygen density for a helium flux of $2\,m^3\,h^{-1}$, an $O_2$ flux of $0.01\,m^3\,h^{-1}$ (corresponds to an $O_2$ admixture of 0.5%) and an RF power of 150 W is shown in figure 15(*b*). Note that if the vastly larger value for the quenching coefficient of $O(3p\,^3P_J)$ atoms by helium from [34] were used, then O atom density values about 3 times higher would result.

The atomic oxygen density and the gas temperature are highest close to the nozzle: $2.8 \times 10^{15}\,cm^{-3}$ and 80°C, respectively. The atomic density decreases by nearly two orders of magnitude, and the gas temperature drops to 65°C over a distance of ∼10 cm on-axis. This observation is in good agreement with the predictions of the one-dimensional model of Jeong *et al* [15] as described in section 1. The atomic density remains sharply concentrated within the nozzle cross section, although the temperature field indicates a slight beam divergence. Only the shape of the radial density distribution develops from a hollow profile, caused by the annular structure of the nozzle, to a centred one at far distances; the particular case of a flat-top density profile is found at ∼1 cm. It is likely that the radial density drop at the beam border is considerably steeper because the laser beam with an estimated diameter of ∼4 mm is not focused in the radial direction for the chosen orientation of the cylindrical lens. The situation is alleviated by the nonlinear character of the two-photon excitation process, which leads to an effective radial resolution of ∼2 mm.

## 6. Conclusion and outlook

Absolute O density measurements have been performed at an RF-excited APPJ using a new TALIF scheme for xenon in which both the two-photon resonance and the fluorescence transition match the corresponding transitions of atomic oxygen. The data required for this calibration of the atomic oxygen ground state density have been determined with the aid of a flow-tube reactor. In particular, the quenching coefficients of $O(3p\,^3P_J)$ atoms in He and Ar, for which some confusion related to the available data base existed, have been re-measured as accurately as possible over the maximum possible pressure interval.

This calibration scheme has been applied to map the absolute atomic oxygen density in the effluent of an APPJ with coaxial geometry operated in an $O_2$/He mixture. The results yield important information about the role of atomic oxygen within the reaction processes running in the jet effluent. Good agreement is found between these measurements and the predictions of Jeong *et al* [15] based on a simplified one-dimensional chemical kinetic model.

We have found, in addition, indications for a local generation of O atoms via other processes: emission of excited O atoms far outside the nozzle (see [7]), as well as a substantial amount of (V)UV radiation, which is actually transmitted through the carrier gas column over considerable distances from the nozzle even in an air environment. Besides ongoing diagnostics like OES in the visible and the (V)UV spectral range as well as laser diode absorption spectroscopy for helium and argon metastables, we are preparing FTIR spectroscopy to diagnose ozone, nitric oxides and hydroxyl molecules to obtain an improved understanding of the reactions in the discharge.

## Acknowledgments

This work was supported by the 'Ministerium für Wissenschaft und Forschung des Landes Nordrhein-Westfalen' in the frame of the 'Verbund Plasmagestützte Oberflächenmodifikation von Medizin- und Biotechnischer Bedeutung—TP 5'. We thank Carola Fischer and Jürgen Leistikow for skillful technical assistance.

## References

[1] Massines F, Rabehi A, Decomps P, Ben Gardi R, Segur P and Mayoux C 1998 *J. Appl. Phys.* **83** 2950–7
[2] Moison M, Zakrzewski Z, Etemadi R and Rostaing J C 1998 *J. Appl. Phys.* **83** 5691–701
[3] Schütze A, Jeong J Y, Babayan S E, Park J, Selwyn G S and Hicks R F 1998 *IEEE Trans. Plasma Sci.* **26** 1685–94
[4] Park J, Henins I, Herrmann H W and Selwyn G S 2001 *J. Appl. Phys.* **89** 15–19
[5] Park J, Henins I, Herrmann H W, Selwyn G S and Hicks R F 2001 *J. Appl. Phys.* **89** 20–8
[6] Park J, Henins I, Herrmann H W and Selwyn G S 2000 *Appl. Phys. Lett.* **76** 288–90
[7] Wang S, Schulz-von der Gathen V and Döbele H F 2003 *Appl. Phys. Lett.* **83** 3272–4
[8] Selwyn G S, Herrmann H W, Park J and Henins I 2001 *Contrib. Plasma Phys.* **41** 610–19
[9] Jeong J Y, Babayan S E, Schütze A, Tu V J, Park J, Henins I, Selwyn G S and Hicks R F 1999 *J. Vac. Sci. Technol.* A **17** 2581–5
[10] Tu V J, Jeong J Y, Schütze A, Babayan S E, Ding G, Selwyn G S and Hicks R F 2000 *J. Vac. Sci. Technol.* A **18** 2799–805
[11] Joeng J Y, Babayan S E, Tu V J, Park J, Henins I, Hicks R F and Selwyn G S 1998 *Plasma Sources Sci. Technol.* **7** 282–5
[12] Babayan S E, Jeong J Y, Tu V J, Park J, Selwyn G S and Hicks R F 1998 *Plasma Sources Sci. Technol.* **7** 286–8
[13] Nowling G R, Babayan S E, Jankovic V and Hicks R F 2002 *Plasma Sources Sci. Technol.* **11** 97–103
[14] Herrmann H W, Henins I, Park J and Selwyn G S 1998 *Phys. Plasmas* **6** 2284–9
[15] Jeong J Y, Park J, Henins I, Babayan S E, Tu V J, Selwyn G S, Ding G and Hicks R F 2000 *J. Phys. Chem.* A **104** 8027–32
[16] Döbele H F 1995 *Plasma Sources Sci. Technol.* **4** 224–33
[17] Döbele H F, Czarnetzki U and Goehlich A 2000 *Plasma Sources Sci. Technol.* **9** 477–91
[18] Bonin K D and McIlrath J 1984 *J. Opt. Soc. Am.* B **1** 52–5
[19] Kohse-Höinghaus K 1994 *Prog. Energy Combust. Sci.* **20** 203–79
[20] Dasch C J and Bechtel J H 1981 *Opt. Lett.* **6** 36–8
[21] Teets R E and Bechtel H 1981 *Opt. Lett.* **6** 458–60
[22] Konz E, Grzeszik R, Marowsky G, Akimov V, Rusin L and Rubahn H G 1997 *Appl. Phys.* B **64** 613–18
[23] Picard Y J, Grisch F, Attal-Tretout B and Le Boiteux S 1997 *Z. Phys.* D **39** 49–58
[24] Dux R, Grützmacher K and de la Rosa M I 1995 *Phys. Rev.* E **51** 1416–27
[25] Goehlich A, Kawetzki T and Döbele H F 1998 *J. Chem. Phys.* **108** 9362–70
[26] Niemi K, Schulz-von der Gathen V and Döbele H F 2001 *J. Phys. D: Appl. Phys.* **34** 2330–5
[27] Clyne M A A and Nip W S 1979 *Reactive Intermediates in the Gas Phase* ed D W Setser (New York: Academic)
[28] Faist M B and Bernstein R B 1976 *J. Chem. Phys.* **64** 2971–84
Faist M B and Bernstein R B 1976 *J. Chem. Phys.* **64** 3924–9
[29] Jeffries J B, Copeland R A and Crosley D R 1989 *J. Chem. Phys.* **91** 2200–5
[30] Feofilov P P 1961 *The Physical Basis of Polarized Emission* (New York: Consultans Bureau)

[31] Sobelman I 1979 *Atomic Spectra and Radiative Transitions* (Berlin: Springer)
[32] Chérigier L, Czarnetzki U, Luggenhölscher D, Schulz-von der Gathen V and Döbele H F 1999 *J. Appl. Phys.* **85** 696–702
[33] Dilecce G, Vigliotti M and De Benedictis S 2000 *J. Phys. D: Appl. Phys.* **33** L53–6
[34] Bittner J, Kohse-Höinghaus K, Meier U and Just Th 1988 *Chem. Phys. Lett.* **143** 571–6
[35] Alekseev V and Setser D W 1996 *J. Phys. Chem.* **100** 5766–80
[36] Inoue G, Ku J K and Setser D W 1984 *J. Chem. Phys.* **81** 5760–74
[37] Bamford D J, Jusinski L E and Bischel W K 1986 *Phys. Rev.* A **34** 185–98
[38] Bruce M R, Layne W B, Whitehead C A and Keto J W 1990 *J. Chem. Phys.* **92** 2917–26
[39] Wells R J 1999 *J. Quant. Spectrosc. Radiat. Transfer* **62** 29–48
[40] Marquardt D W 1963 *J. Soc. Indust. Appl. Math.* **11** 431–41
[41] Saxon R and Eichler J 1986 *Phys. Rev.* A **34** 199–206
[42] Omidvar K 1980 *Phys. Rev.* A **22** 1576–87
Omidvar K 1984 *Phys. Rev.* A **30** 2805(E)
[43] Pindzola M S 1978 *Phys. Rev.* A **17** 1021–7
[44] Miller J C 1989 *Phys. Rev.* A **40** 6969–76
[45] Horiguchi H, Chang R S F and Setser D W 1981 *J. Chem. Phys.* **75** 1207–18
[46] Amorim J, Baravian G and Sultan G 1996 *Appl. Phys. Lett.* **68** 1915–7
[47] Dunlop J R, Tserepi A D, Prepernau B L and Miller T A 1992 *Plasma Chem. Plasma Process.* **12** 89–101